

# Monte Carlo Simulations of Absorption and Fluorescence Spectra in Ellipsoidal Nanocavities

J. A. Gomez and Ward H. Thompson\*

Department of Chemistry, University of Kansas, Lawrence, Kansas 66045

Received: February 29, 2004; In Final Form: June 18, 2004

The absorption and fluorescence spectra of a model solute molecule dissolved in a CH<sub>3</sub>I solvent confined in nanoscale ellipsoidal cavities have been simulated for solutions with densities equal to 1.4, 2.0, and 2.2 g/cm<sup>3</sup>. The model solute is a diatomic molecule with an electronic charge-transfer transition. Monte Carlo simulations have been performed for solutions confined in hydrophobic prolate and oblate ellipsoidal cavities of varying size. The results of the absorption and fluorescence spectra are compared with previous simulations of confined solvents in spherical cavities. The solute and solvent molecule probability density distributions have been calculated and are used to interpret the spectra. An umbrella sampling approach is used to obtain accurate results for the solute probability distributions.

## 1. Introduction

Advances in synthetic techniques have made it possible to generate confined solvent systems with a wide variety of properties.<sup>1–6</sup> Among the confining frameworks that have been the subject of recent study are sol–gels,<sup>1,7–12</sup> reverse micelles,<sup>2,13–18</sup> zeolites,<sup>19</sup> proteins, and supramolecular assemblies.<sup>3</sup> These systems are of interest for a variety of potential applications including catalysis, sensors, and separations as well as understanding systems occurring in nature.<sup>21</sup> However, these confining structures are extremely diverse, varying widely in dimensionality (e.g., cavities versus pores), size, shape, surface roughness, surface flexibility, and chemical functionality, and the chemical dynamics is frequently complex. Thus, developing general principles for designing confining frameworks that will serve a specific purpose (e.g., a microporous catalyst) is not a simple task. Simulations provide an important complement to experimental measurements since the cavity or pore characteristics can be explicitly controlled and the effects of each property on chemistry occurring in the confined solvent determined.<sup>6,15–26</sup>

Recently, we have simulated the charge-transfer spectra<sup>25</sup> and time-dependent fluorescence<sup>26</sup> (TDF) of a model dye molecule inside spherical, hydrophobic nanocavities as a function of cavity size. These processes are interesting both for comparisons with experimental measurements and for insights into charge-transfer reactions (e.g., electron or proton transfer) that involve similar solvent reorientational dynamics. In addition, charge transfer processes are, in general, strongly affected by solvent confinement since they are intimately coupled to the solvent dynamics. Our previous simulations found that the distribution of solute positions inside the cavity is an important variable that impacts both steady-state spectra<sup>25</sup> and time-dependent fluorescence.<sup>26</sup> Specifically, the solute dye molecule has a significantly larger dipole moment in the excited state compared to the ground state. This leads to an excited state solute position distribution that is peaked in the cavity interior (a fully solvated solute) and a ground state position distribution peaked near the cavity wall (a half-solvated solute). The corresponding fluorescence spectra are therefore sensitive to the changes in effective solvent polarity that occur upon changing the cavity size, while the absorption spectra are relatively insensitive to the same changes: the

fluorescence spectra shift consistently to the red (longer wavelength) as the cavity size is increased, while the absorption spectra are essentially unchanged. The difference in ground and excited-state position distributions led to the prediction that solute motion may contribute to the time-dependent fluorescence signal.<sup>25</sup> This prediction was verified using nonequilibrium molecular dynamics simulations.<sup>26</sup>

In this paper we extend our Monte Carlo simulations of the steady-state spectra of a dye molecule in spherical nanoscale cavities to ellipsoidal cavities. Thus, we move beyond the consideration of cavity size to examine the effect of changing cavity shape and, naturally, the breaking of spherical symmetry. We consider both prolate and oblate ellipsoidal cavities of varying size (beginning from the spherical case). The solute–solvent system is the same as in previous work<sup>25,26</sup> and is outlined in section 2 along with the extension of the cavity model to ellipsoids. The details of the Monte Carlo simulations including the umbrella sampling approach necessary to obtain accurate solute position distributions are described in section 3. The solvent and solute position distributions along with the steady-state absorption and fluorescence spectra are presented and discussed in section 4. Finally, some concluding remarks are given in section 5.

## 2. Interaction Potential

**2.1. Potential Form.** We have carried out Monte Carlo simulations for a model solute molecule dissolved in a CH<sub>3</sub>I solvent confined in ellipsoidal cavities. The solute is a model diatomic molecule (denoted as AB), with an electronic charge-transfer transition. The electronic structure of the solute is described in terms of a two valence bond state model with electronic coupling of only 0.01 eV so that the ground and the excited states have effectively fixed charges with molecular dipoles of 1.44 and 7.2 D, respectively. The excited state is 2 eV higher in energy than the ground state. The CH<sub>3</sub>I solvent molecules are also considered as diatomic molecules with fixed molecular dipole equal to 2.6 D.<sup>27</sup> The methyl groups in the solvent are treated as “unified atoms.” Both solute and solvent are rigid molecules.

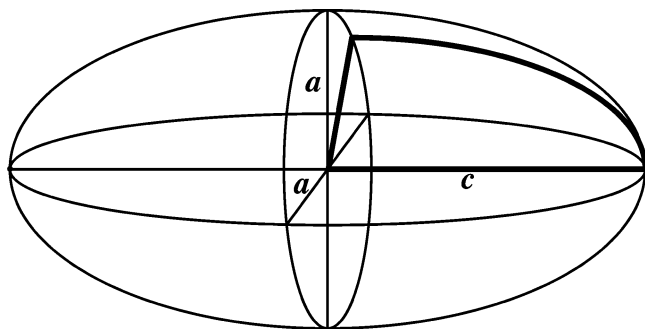


**Figure 1.** A prolate ellipsoid is shown with the minor semi-axes  $a$  and the major semi-axis  $c$  indicated. The bold lines outline the region in which the interaction potential integrals, eq 5, are mapped.

The solute AB interacts with the  $\text{CH}_3\text{I}$  solvent molecules through Lennard-Jones and Coulomb potentials. The Lennard-Jones parameters for atoms A and B are the same and independent of the electronic state. The interactions of the solute and solvent molecules with the cavity wall involve a Lennard-Jones interaction. A general expression for the total potential energy for a system of  $N$  molecules confined in a cavity is given by

$$V(\mathbf{R}) = \sum_{i=1}^{N-1} \sum_{j>1}^N \sum_{\alpha_i=1}^{n_i} \sum_{\alpha_j=1}^{n_j} \left[ u_{\text{LJ}}(r_{\alpha_i\alpha_j}) + \frac{q_{\alpha_i}q_{\alpha_j}}{r_{\alpha_i\alpha_j}} \right] + \sum_{i=1}^N \sum_{\alpha_i=1}^{n_i} u_{\text{LJ}}^{\text{ws}}(\mathbf{r}_{\alpha_i}) \quad (1)$$

where  $n_i$  is the number of atoms (or interaction sites) in molecule  $i$ ,  $r_{\alpha_i\alpha_j}$  denotes the distance between atoms  $\alpha_i$  and  $\alpha_j$  on molecules  $i$  and  $j$ ,  $\mathbf{r}_{\alpha_i}$  denotes the position of atom  $\alpha_i$  with respect to the center of the cavity, and  $q_{\alpha_i}$  is the charge of atom  $\alpha_i$ . The first term in eq 1 gives the contribution to the total potential energy due to the intermolecular interactions while the second term gives the contribution due to the molecule–cavity wall interactions. The Lennard-Jones potential energy between molecules is given by

$$u_{\text{LJ}}(r_{\alpha_i\alpha_j}) = 4\epsilon_{\alpha_i\alpha_j} \left[ \left( \frac{\sigma_{\alpha_i\alpha_j}}{r_{\alpha_i\alpha_j}} \right)^{12} - \left( \frac{\sigma_{\alpha_i\alpha_j}}{r_{\alpha_i\alpha_j}} \right)^6 \right] \quad (2)$$

where  $\sigma_{\alpha_i\alpha_j}$  and  $\epsilon_{\alpha_i\alpha_j}$  represent, respectively, the Lennard-Jones diameter and well-depth parameter. The terms  $u_{\text{LJ}}^{\text{ws}}(\mathbf{r}_{\alpha_i})$  are the Lennard-Jones interactions of atoms with the cavity wall and are explained in detail in section 2.2. The model parameters for solute<sup>25</sup> and solvent molecules<sup>27</sup> are the same as those used in previous work<sup>25</sup> and are given in Table 1.

## 2.2. Molecule–Wall Interactions for Ellipsoidal Cavities.

A number of previous works<sup>17,18,22,23</sup> have considered molecules confined inside smooth spherical cavities. When molecules interact with these cavity walls via a Lennard-Jones interaction, the result is a potential energy that depends only on the distance of each interaction site in a molecule from the center of the cavity.<sup>15,16</sup> Due to the spherical symmetry, structural properties of molecules need only be examined as a function of radial coordinates. In this work, we examine the effects of breaking the spherical symmetry by considering ellipsoidal cavities. We consider prolate and oblate ellipsoidal cavities with the wall defined by

$$\frac{(x^2 + y^2)}{a^2} + \frac{z^2}{c^2} = 1 \quad (3)$$

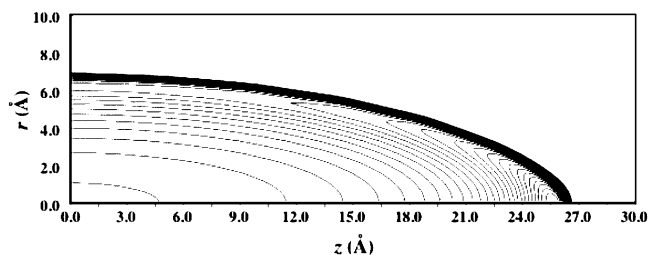


**Figure 2.** The interaction energy of an iodine atom with the ellipsoidal cavity wall ( $a = 10$  Å,  $c = 30$  Å) is shown as a function of the atom position in a plane. Thirty contours are shown from  $-1.69$  to  $0.0$  kcal/mol.

where  $a$  and  $c$  are the semi-axes of the ellipsoidal cavity (see Figure 1). A spherical cavity is obtained when  $a = c$  and  $c > a$  ( $c < a$ ) gives a prolate (oblate) ellipsoid.

In the calculation of the Lennard-Jones interaction between the molecules and cavity wall, it is assumed that the region exterior to the cavity consists of a uniform density  $\rho$  of continuum sites. The Lennard-Jones parameters for the cavity wall are the same used in previous work:<sup>16–18,25</sup>  $\sigma_{\text{Wall}} = 2.5$  Å,  $\epsilon_{\text{Wall}} = 0.46$  kcal/mol. The result of this interaction at the site position  $\mathbf{r}$  inside the cavity is given by the following expression:

$$u_{\text{LJ}}^{\text{ws}}(\mathbf{r}) = 4\rho\epsilon_{\text{Wall}}[\sigma_{\text{Wall}}^{12}I(\mathbf{r}, 12) - \sigma_{\text{Wall}}^6I(\mathbf{r}, 6)] \quad (4)$$

where

$$I(\mathbf{r}, n) = \int_{\Omega} \frac{d^3\mathbf{r}_o}{|\mathbf{r} - \mathbf{r}_o|^n} \quad (5)$$

Here  $\mathbf{r}$  is the site position relative to the center of the cavity and  $\mathbf{r}_o$  ranges over the region  $\Omega$  exterior to the cavity. Note that the values of the integrals  $I(\mathbf{r}, n)$  ( $n = 6, 12$ ) depend on the semi-axes  $a$  and  $c$ . In contrast to the spherical cavity case, there is no closed expression that represents the interaction potential  $u_{\text{LJ}}^{\text{ws}}$  for ellipsoidal cavities. Hence, the integral in eq 5 must be solved by numerical methods. Since these are multi-dimensional integrals, appropriate algorithms include Gaussian<sup>29</sup> and pseudo-random<sup>30</sup> methods. We used a pseudo-random approach, which we find to be more stable than Gaussian methods. In this method, the grid of points over the region  $\Omega$  is generated with the Diophantine method,<sup>30</sup> which is pseudo-random in the sense that the same “random” point distribution is obtained for the same set of initial parameters.

As an example of the numerical calculation of the potential  $u_{\text{LJ}}^{\text{ws}}$  with  $I(\mathbf{r}, n)$ , consider an iodine atom interacting with the wall of an ellipsoidal cavity of semi-axes  $a = 10$  Å and  $c = 30$  Å. The atom–wall interaction energies for this case are shown as a contour plot in Figure 2 as a function of the atomic position in the plane of symmetry (see Figure 1). It is clear from this figure that the potential energy has a deeper well near the cavity wall along the (long) semi-axis  $c$ . This example illustrates that in the model cavity the interaction potential  $u_{\text{LJ}}^{\text{ws}}$  is anisotropic around the center of the ellipsoidal cavity.

The interaction potential must be calculated many millions (or even billions) of times in a Monte Carlo simulation. To render this tractable, the values of the integrals  $I(\mathbf{r}, n)$  ( $n = 6, 12$ ) are mapped on a plane that contains the main semi-axis as is shown in Figure 1. (The symmetry about the main semi-axis  $c$  is used.) In this symmetry plane, the mapping was done by using radial and angular polar coordinates. In actual calculations, we employed a very dense mapping: 300 and 200 points for the radial and angular coordinates, respectively. From

**TABLE 1: Parameters for the Interaction Models of the Solute and Solvent Molecules Used in the Monte Carlo Simulations<sup>a</sup>**

site	$\epsilon$ (kcal/mol)	$\sigma$ (Å)	q	$r_{ij}$ (Å)
Solute				
ground state				
A	0.3976	3.5	+0.1	3.0
B	0.3976	3.5	−0.1	
excited state				
A	0.3976	3.5	+0.5	3.0
B	0.3976	3.5	−0.5	
Solvent				
CH <sub>3</sub> I (ref 27)				
CH <sub>3</sub>	0.2378	3.77	+0.25	2.16
I	0.5985	3.83	−0.25	

<sup>a</sup> The parameters  $\epsilon$  and  $\sigma$  define the Lennard-Jones interactions,  $q$  the site charge, and  $r_{ij}$  the distance between the site listed and the previous site.

**TABLE 2: Number of Molecules,  $N$ , in the Nanocavity for Three Densities as a Function of the Semi-Axes  $a$  and  $c$ <sup>a</sup>**

cavity dimensions (Å)	$N$		
	1.4 g/cm <sup>3</sup>	2.0 g/cm <sup>3</sup>	2.2 g/cm <sup>3</sup>
$a=10, c=10$	16	23	26
$a=10, c=15$	25	71	39
$a=10, c=30$	50	63	78
$a=10, c=50$	83	119	131
$a=15, c=10$	37	53	
$a=30, c=10$	150	257	

<sup>a</sup> The number includes the solvent molecules and the single solute molecule

this mapping, we performed a two-dimensional linear interpolation for computing the values of the integrals  $I(\mathbf{r}, n)$  at the site position  $\mathbf{r}$  at each Monte Carlo step. With this methodology, the complex integrals in eq 5 only need to be computed once for constructing a database for the values of  $I(\mathbf{r}, n)$  for the desired cavity size. Performing linear interpolations at site positions is much faster than repeated numerical integration.

### 3. Monte Carlo Simulations

We have carried out Monte Carlo simulations to obtain the solute absorption and fluorescence spectra and the probability density distributions and free energies for the solute and solvent molecules. All simulations were carried out at a temperature of 298 K. Several cavity sizes have been considered and three solution densities examined for each cavity size. The number of molecules for each cavity size and solution density are given in Table 2. (The volume used for calculating the densities is obtained by reducing the semi-axis  $a$  by  $0.5\sigma_{\text{wall}}$  and the semi-axis  $c$  by  $0.5\sigma_{\text{wall}}(c/a)$  in the prolate ellipsoid case and  $a$  by  $0.5\sigma_{\text{wall}}$  and  $c$  by  $0.5\sigma_{\text{wall}}(a/c)$  in the oblate ellipsoid case.)

In each Monte Carlo simulation, the confined solution is initiated from a bulk configuration large enough to select the number of desired molecules,  $N$ . The initial cavity size is made large enough to include  $N$  molecules (typically with dimensions larger than the desired semi-axes  $a$  and  $c$ ). The initial size of the semi-axes are then reduced in the warm-up step by 0.1 Å in the direction of semi-axis  $a$  and  $(c/a)*0.1$  Å in the direction of semi-axis  $c$  every 100 cycles (1 cycle =  $N$  steps) until the semi-axes of the cavity reach the desired size. The equilibration continues until a total of 400 000 cycles is completed. Subsequently, 6 000 000 cycles are used for the data collection period.

In the warm-up when the cavity size is being reduced, the Lennard-Jones interaction potential  $u_{\text{LJ}}^{\text{ws}}$  is calculated using eq 4 by performing numerical integration of the integral in eq 5. Once

the cavity reaches the desired size, a symmetry plane is chosen (Figure 1) over which values for the integrals  $I(\mathbf{r}, n)$  ( $n = 6, 12$ ) are mapped. Thereafter, numerical interpolation is performed to compute the values of the integrals  $I(\mathbf{r}, n)$  ( $n = 6, 12$ ) in subsequent cycles. This approach is used even for the spherical cavity ( $a = c$ ) case.

**3.1. Absorption and Fluorescence Spectra.** The absorption and fluorescence spectra were calculated by the Golden Rule approach, in which the spectral intensity is given by<sup>28</sup>

$$I(\omega) \propto \langle |\mu_{\text{ex,gr}}|^2 \delta(E_{\text{ex}} - E_{\text{gr}} - \hbar\omega) \rangle \quad (6)$$

where  $\langle \dots \rangle$  indicates a thermal average with the solute in the ground (excited) state for the absorption (fluorescence) spectrum and  $\mu_{\text{ex,gr}}$  is the transition dipole moment in the two valence bond state model. Due to the small electronic coupling,  $\mu_{\text{ex,gr}}$  is roughly constant. Thus the spectrum is essentially the distribution of energy gaps,  $E_{\text{gr}} - E_{\text{ex}}$ , experienced by the solute due to the interactions with the solvent. The spectra are therefore calculated in the slow modulation limit, an approximation that is generally valid for dipolar solutes in polar solvents. From eq 1, it is clear that the Lennard-Jones interactions (both molecule–molecule and molecule–wall) do not contribute to the energy gap because the AB Lennard-Jones parameters are the same in the ground and excited states. The contributions to the energy gap come from the Coulomb interaction that includes only terms involving the solute molecule. We are only interested in the position and width of the spectra, not in the relative intensities. Hence, the proportionality constant in eq 6 is taken such that  $I(\omega_{\text{max}}) = 1$ , where  $\omega_{\text{max}}$  is the frequency at which the intensity is a maximum.

The absorption and fluorescence spectra were also calculated in bulk solution for comparison with the cavity simulations. Specifically, one solute and 255 solvent molecules were simulated with periodic boundary conditions using a cubic simulation box for densities of 1.4, 2.0, and 2.2 g/cm<sup>3</sup>; an Ewald summation was used to account for the long-range electrostatic interactions.<sup>31,32</sup> Each spectrum was calculated after a 100 000 cycle equilibration from a 1 000 000 cycle run. In all other respects the simulations were identical to those in the cavities.

**3.2. Probability Density and Free Energy of Solute.** To obtain the probability density distribution and free energy as a function of solute molecule position, we employed the umbrella sampling method<sup>31,32</sup> combined with the weighted histogram analysis method (WHAM) of Kumar et al.<sup>33</sup>

In a single Monte Carlo simulation, the computation of the solute probability density can be obtained by constructing histograms that record the frequency of occurrence of particular values of the solute coordinates. In a canonical ensemble for a system of  $N$  molecules at a constant temperature and volume, the average solute density distribution as a function of, for example, the center-of-mass  $\mathbf{r}_{\text{CM}}$  can be expressed by

$$P(\mathbf{r}_{\text{CM}}) = \frac{\int d\mathbf{R} \delta[\xi(\mathbf{R}) - \mathbf{r}_{\text{CM}}] e^{-\beta V(\mathbf{R})}}{\int d\mathbf{R} e^{-\beta V(\mathbf{R})}} \quad (7)$$

where  $V(\mathbf{R})$  is the potential energy of the system, eq 1,  $\xi(\mathbf{R})$  is the solute center-of-mass function,  $\beta = 1/k_{\text{B}}T$ , and  $k_{\text{B}}$  is Boltzmann's constant. The (Helmholtz) free energy can then be obtained from the solute density distribution by the expression

$$A(\mathbf{r}_{\text{CM}}) = -k_{\text{B}}T \ln P(\mathbf{r}_{\text{CM}}) \quad (8)$$

However, calculation of the free energy with this approach can

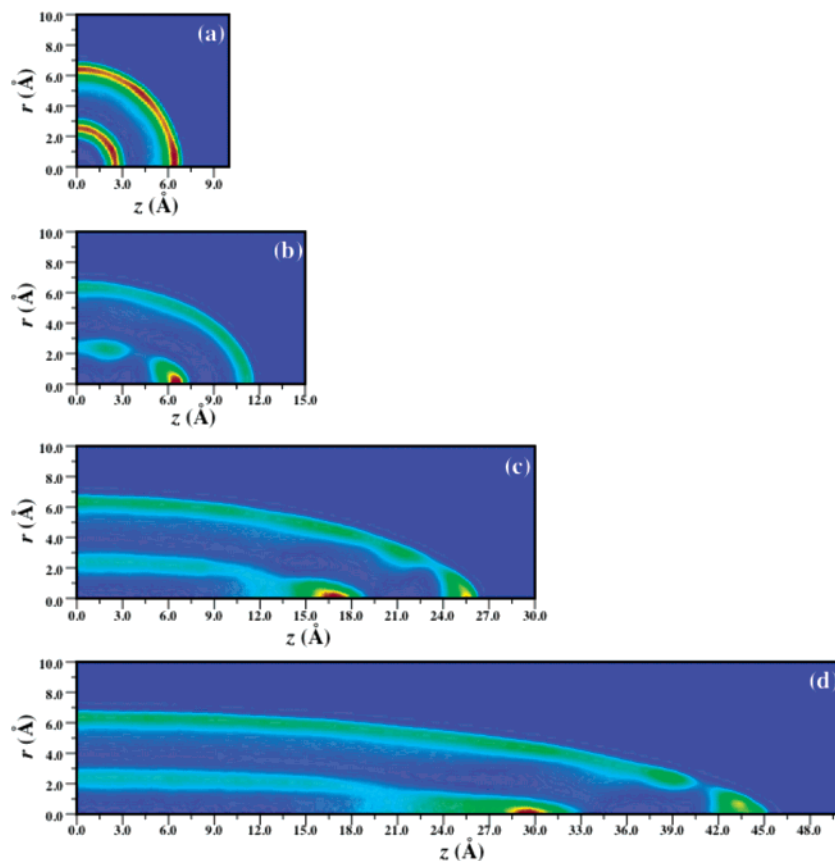


**Figure 3.** The solvent probability density is shown for cavities with  $a = 10$  Å and  $c = 10, 15, 30$ , and  $50$  Å (panels (a), (b), (c), and (d), respectively) for a solution density of  $\rho = 2.0$  g/cm<sup>3</sup>. (These results were obtained with a ground-state solute molecule.) In each plot 100 contours are used between 0 (blue) and the maximum probability density (red) of (a)  $0.084$  Å<sup>-3</sup>, (b)  $0.197$  Å<sup>-3</sup>, (c)  $0.164$  Å<sup>-3</sup>, and (d)  $0.163$  Å<sup>-3</sup>.

be problematic. The difficulty is that the large values of the free energy involve configurations where the solute density is very small, while the sampling is highly concentrated in configurations with low free energy. This can result in high statistical error in the free energies away from the minima. One way to achieve accurate sampling for all configurations of the system and hence the free energies is by using the umbrella sampling scheme proposed by Torrie and Valleu.<sup>34</sup> It consists of adding a biasing potential  $V_{\text{umb}}^i(\xi(\mathbf{R}))$  to the potential of the system  $V(\mathbf{R})$  for concentrating the sampling of configuration space where the solute molecule is in a particular region of the cavity. This scheme is useful whenever it is desired to enhance sampling in configuration space that is scarcely visited by the solute molecule in a simulation. We performed a series of simulations adding biasing potentials for concentrating sampling in different, but overlapping, regions of the configuration space or “windows.” In each simulation, biased solute density distributions are constructed in the form of histograms that can then be pieced together.

The biased solute density distribution with total potential energy  $V(\mathbf{R}) + V_{\text{umb}}^i(\xi(\mathbf{R}))$  is given by

$$P_{\text{biased}}^i(\mathbf{r}_{\text{CM}}) = \frac{\int d\mathbf{R} \delta[\xi(\mathbf{R}) - \mathbf{r}_{\text{CM}}] e^{-\beta[V(\mathbf{R}) + V_{\text{umb}}^i(\xi(\mathbf{R}))]}}{\int d\mathbf{R} e^{-\beta[V(\mathbf{R}) + V_{\text{umb}}^i(\xi(\mathbf{R}))]}} = \frac{e^{-\beta V_{\text{umb}}^i(\mathbf{r}_{\text{CM}})} P_{\text{unbiased}}^i(\mathbf{r}_{\text{CM}})}{\langle e^{-\beta V_{\text{umb}}^i(\xi(\mathbf{R}))} \rangle_{\text{unbiased}}} \quad (9)$$

where  $P_{\text{unbiased}}^i(\mathbf{r}_{\text{CM}})$  is the solute density distribution in the unbiased system, i.e., with total potential energy  $V(\mathbf{R})$ , but

accurate only in a restricted region of the cavity determined by the biased potential, and the denominator is an average computed with the unbiased potential.

The reconstruction of the full, unbiased solute density distribution  $P(\mathbf{r}_{\text{CM}})$  from the separate biased distributions  $P_{\text{unbiased}}^i(\mathbf{r}_{\text{CM}})$  for all the windows in a given cavity is a crucial step and can be difficult when  $\mathbf{r}_{\text{CM}}$  represents more than one degree of freedom (as it does here). To appropriately merge the separate overlapping biased density distributions, we used the weighted histogram analysis method proposed by Kumar et al.<sup>33</sup> Specifically, we carried out a set of  $M$  simulations at the same temperature  $T$  with different biasing potentials. The biasing potentials used in all simulations were explicit functions of the solute coordinates alone (see below). With these features, the WHAM equations employed to compute the complete, unbiased solute density distribution are

$$P(\mathbf{r}_{\text{CM}}) = \frac{\sum_{i=1}^M m_i P_{\text{biased}}^i(\mathbf{r}_{\text{CM}})}{\sum_{i=1}^M m_i e^{-\beta[V_{\text{umb}}^i(\mathbf{r}_{\text{CM}}) - f_i]}} \quad (10)$$

and

$$e^{-\beta f_i} = \int d\mathbf{r} P(\mathbf{r}) e^{-\beta V_{\text{umb}}^i(\mathbf{r})} \quad (11)$$

where  $f_i$  is the window free energy of the  $i$ th biased simulation and represents the shift needed to make the full, unbiased solute density distribution continuous;  $m_i$  is the length of the  $i$ th



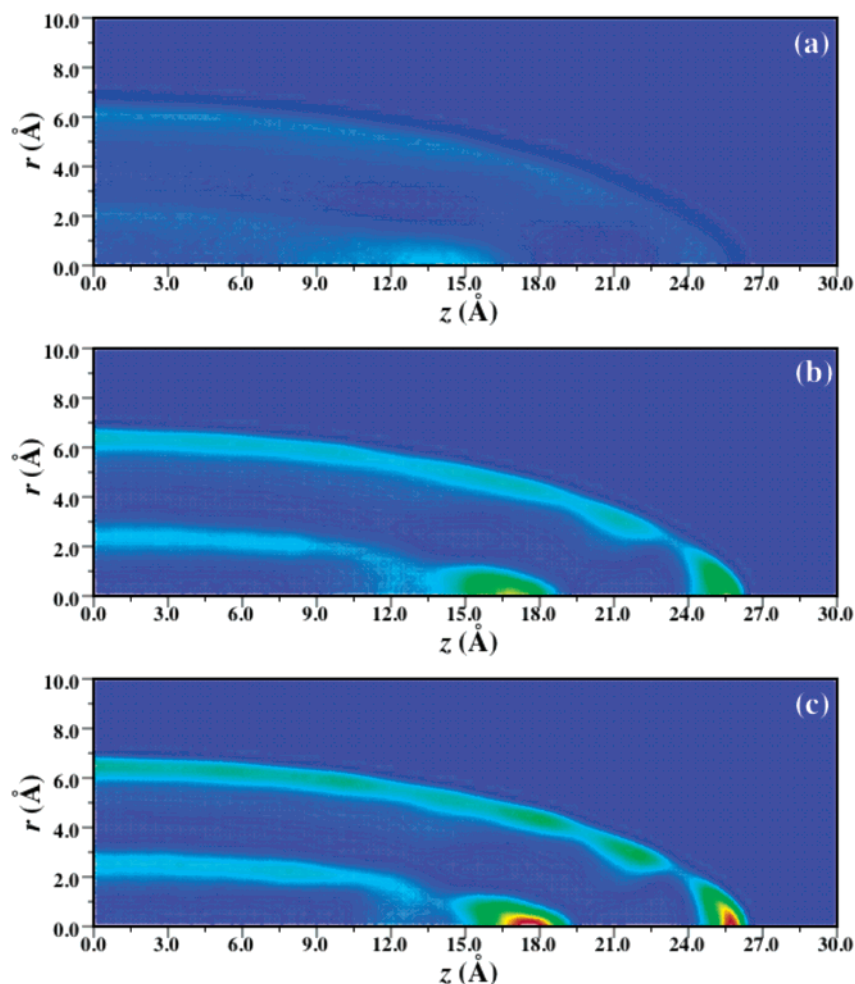


**Figure 4.** The solvent probability density is shown for a cavity with  $a = 10$  Å and  $c = 30$  Å for solution densities of  $\rho = 1.4, 2.0$ , and  $2.2$  g/cm<sup>3</sup> (from top to bottom). (These results were obtained with a ground-state solute molecule.) In each plot 100 contours are used between 0 (blue) and  $0.23$  Å<sup>-3</sup> (red).

simulation, i.e., the number of configurations or steps used to compute  $P_{\text{biased}}^i(\mathbf{r})$ . Equations 10 and 11 provide a way to compute the density distribution  $P(\mathbf{r}_{\text{CM}})$  and thereby the free energy. Since,  $P(\mathbf{r}_{\text{CM}})$  and the set of free energies  $f_i$  are unknown initially, these equations must be solved iteratively. A first guess for the  $\{f_i\}_{i=1}^M$  set (initial values are equal to zero) is used in eq 10 for computing  $P(\mathbf{r}_{\text{CM}})$  in the whole range of configuration space of the solute. Then, the computed  $P(\mathbf{r}_{\text{CM}})$  is used in eq 11 to compute a new set of values for the  $\{f_i\}_{i=1}^M$ , and the process is repeated until convergence is reached.

We have used biasing potentials that are explicit functions of atomic positions of the solute molecule. Since in prolate and oblate ellipsoidal cavities there is symmetry (even in the case of a charged cavity wall) around the main semi-axis, we used cylindrical coordinates for the configuration space of the solute. The  $z$  coordinate of the solute position is taken to be along the main semi-axis,  $c$ , and the  $r$  coordinate is the distance of the solute position from the main semi-axis. Therefore, our density distributions are displayed as a function of the coordinates  $z$  and  $r$ :  $P(z, r)$ .

In this coordinate system, the form of the biasing potential is an explicit function in the coordinates  $z$  and  $r$  and the biasing potential is written as a contribution of two terms,

$$V_{\text{umb}}^i(z, r) = \frac{1}{2}k_z(z - z^i)^2 + \frac{1}{2}k_r(r - r^i)^2 \quad (12)$$

where  $k_z$  and  $k_r$  are force constants and  $z^i$  and  $r^i$  are reference values of the coordinates for the  $i$ th simulation. With the biasing potential of eq 12, we can generate the biased probability distribution  $P_{\text{biased}}^i(z, r)$  concentrated around the reference coordinate  $(z_i, r_i)$ . Once we have reconstructed the full unbiased probability density  $P(z, r)$  by replacing the  $P_{\text{biased}}^i(z, r)$  and  $V_{\text{umb}}^i(z, r)$  sets in eqs 10 and 11, the free energy is obtained by using eq 8. We applied this biasing potential to the coordinates of the center-of-mass of the solute molecule.

The force constants were taken to be  $k_z = k_r = 8.0$  kJ/mol/Å<sup>2</sup> in all the simulations. The reference values of the coordinates  $z^i$  and  $r^i$  were separated by 1 Å in each coordinate with the range of variation depending on cavity size. Each Monte Carlo simulation to calculate the biased solute density distribution  $P_{\text{biased}}^i(z, r)$  consisted of 400 000 equilibration cycles and 4 000 000 cycles.

#### 4. Results and Discussion

In this section we present results from the Monte Carlo simulations described in section 3. Specifically, the solvent and solute probability densities and absorption and fluorescence spectra in the spherical and ellipsoidal nanoscale cavities are shown and discussed. We begin by examining the solvent densities that are important for understanding everything that follows. The absorption and fluorescence spectra are then presented and interpreted based on the solute position distributions.

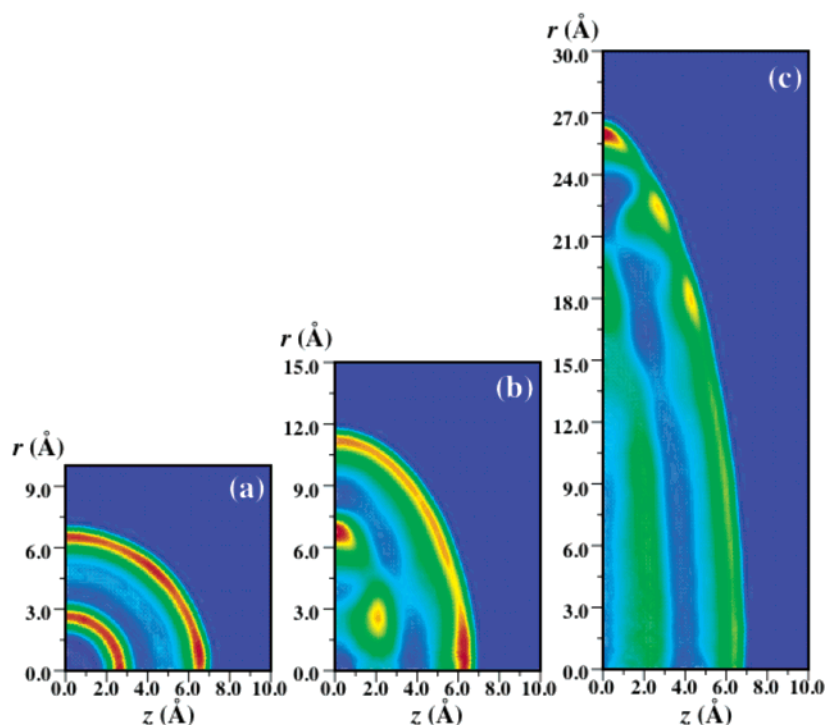


**Figure 5.** The solvent probability density is shown for cavities with  $a = 10, 15$ , and  $30 \text{ \AA}$  (from left to right) and  $c = 10 \text{ \AA}$  for a solution density of  $\rho = 2.0 \text{ g/cm}^3$ . (These results were obtained with a ground-state solute molecule.) In each plot 100 contours are used between 0 (blue) and the maximum probability density (red) of (a)  $0.142 \text{ \AA}^{-3}$ , (b)  $0.062 \text{ \AA}^{-3}$ , and (c)  $0.085 \text{ \AA}^{-3}$ .

**4.1. Solvent Probability Density.** *4.1.1. Prolate Ellipsoidal Cavities.* The solvent probability density as a function of the cylindrical coordinates  $z$  and  $r$  (see section 3.2) is shown in Figure 3 for prolate ellipsoidal cavities with semi-axis  $a$  fixed at  $10 \text{ \AA}$  and the semi-axis  $c$  equal to  $10, 15, 30$ , and  $50 \text{ \AA}$  for solutions with density equal to  $2.0 \text{ g/cm}^3$ . A comparison of the solvent probability densities in cavities with  $a = 10 \text{ \AA}$  and  $c = 30 \text{ \AA}$  and solution densities of  $1.4, 2.0$ , and  $2.2 \text{ g/cm}^3$  is given in Figure 4. The solvent probability densities were simulated with the solute molecule in the ground state. Solvent densities with the solute molecule in the excited state are very similar to those shown in Figures 3 and 4. The solvent probability density,  $P_{\text{solv}}(z, r)$ , is normalized to the number of solvent molecules so that

$$\int_0^c dz \int_0^{a\sqrt{1-z^2/c^2}} 2\pi r dr P_{\text{solv}}(z, r) = N - 1 \quad (13)$$

where  $N$  is the total number of molecules including the solute (see Table 2).

From Figures 3 and 4, a layered structure of the solvent density parallel to the cavity surface can be clearly seen. The magnitude of the density oscillations increases with the solution density. For the spherical cavity ( $a = c = 10 \text{ \AA}$ ), we can see that the solvent probability density has spherical symmetry. For this cavity, there are two layered regions: one of high probability density near the cavity wall and the other near the center of the cavity. For the prolate ellipsoidal cavities, two layered regions of high probability density are also observed, but in these cavities the density peaks on the main semi-axis  $c$  in the intervals  $z = 5\text{--}7, 13.5\text{--}18$ , and  $22.5\text{--}31 \text{ \AA}$  for cavities with  $c = 15, 30$ , and  $50 \text{ \AA}$ , respectively. It can be seen from Figure 4 that the maximum peaks of the probability density shift toward the cavity wall as the solution density increases. The separation between the solvent layers is approximately  $4 \text{ \AA}$ , which is similar to the Lennard-Jones diameter for the solvent molecule (see

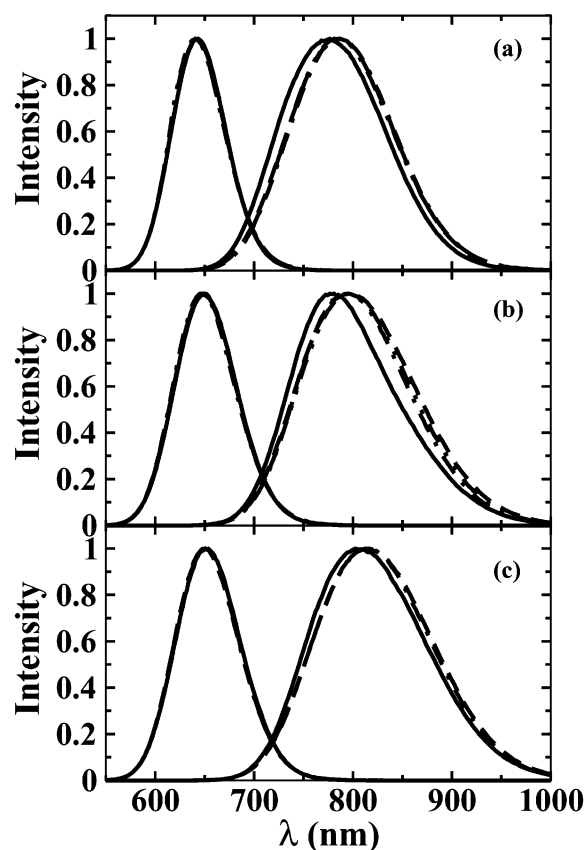


**Figure 6.** The absorption and fluorescence spectra are plotted for prolate ellipsoidal cavities with  $a = 10 \text{ \AA}$  and  $c = 10$  (solid lines),  $15$  (dashed lines),  $30$  (dot-dashed lines), and  $50 \text{ \AA}$  (dot-dot-dashed lines) for solution densities of (a)  $1.4 \text{ g/cm}^3$ , (b)  $2.0 \text{ g/cm}^3$ , and (c)  $2.2 \text{ g/cm}^3$  ( $c = 10, 15$ , and  $30 \text{ \AA}$  only). All of the absorption spectra and the fluorescence spectra for  $c \geq 15 \text{ \AA}$  are plotted but are difficult to distinguish due to their strong similarity; see Table 3.

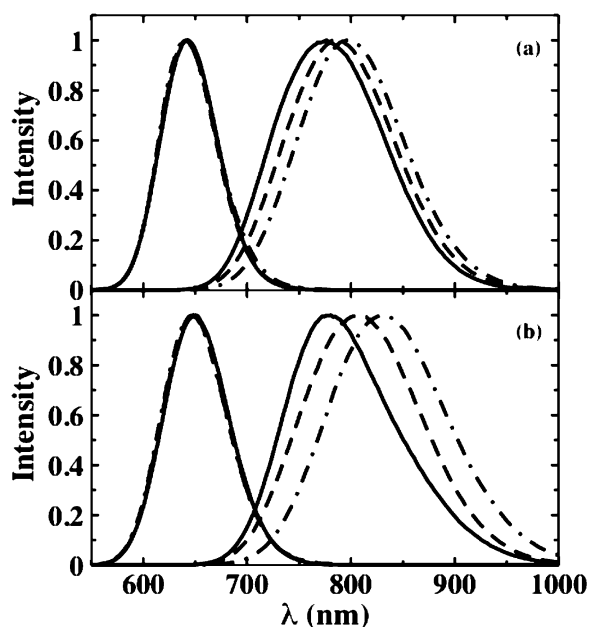


**Figure 7.** The absorption and fluorescence spectra are plotted for oblate ellipsoidal cavities with  $c = 10$  Å and  $a = 10$  (solid lines), 15 (dashed lines), and 30 Å (dot-dashed lines) for solution densities of (a) 1.4 g/cm<sup>3</sup>, and (b) 2.0 g/cm<sup>3</sup>. As in Figure 6, all the absorption spectra are plotted but are difficult to distinguish.

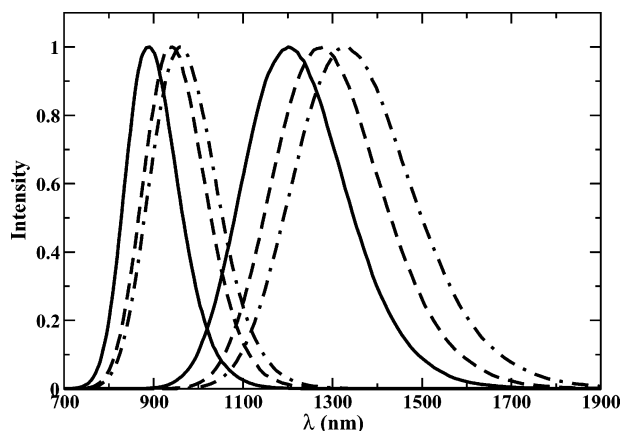


**Figure 8.** The absorption and fluorescence spectra are plotted for bulk solution solution densities of 1.4 (solid lines), 2.0 (dashed lines), and 2.2 g/cm<sup>3</sup> (dot-dashed lines).

Table 1). It is also worth noting that the shape of the layered structure tends toward cylindrical symmetry as the main semi-axis increases. This is clearly seen at regions near the middle (small  $z$ ) of the biggest cavities.

**4.1.2. Oblate Ellipsoidal Cavities.** The solvent probability density for oblate ellipsoidal cavities with the main semi-axis  $c$  fixed to 10 Å and the semi-axis  $a$  equal to 10, 15, and 30 Å for a density of 2.0 g/cm<sup>3</sup> is shown in Figure 5. These solvent probability densities were simulated with the solute in the ground state and also were normalized according to eq 13. From this figure we can also see the layered structure of the solvent probability density parallel to the cavity surface with two regions of high probability density. The separation of these two layers is approximately 4 Å, again similar to the Lennard-Jones diameter for the solvent molecule.

**4.2 Absorption and Fluorescence Spectra.** **4.2.1. Prolate Ellipsoidal Cavities.** The absorption and fluorescence spectra for the solute molecule in CH<sub>3</sub>I solvent confined in prolate ellipsoidal cavities with semi-axes  $a = 10$  Å and  $c = 10, 15,$

**TABLE 3: Position of the Maximum,  $\lambda_{\text{max}}$ , and the Full-Width at Half-Maximum (fwhm) of the Absorption and Fluorescence Spectra for the Model AB Solute Molecule for Different Cavity Sizes and Solution Densities<sup>a</sup>**

cavity dimensions (Å)	1.4 g/cm <sup>3</sup>		2.0 g/cm <sup>3</sup>		2.2 g/cm <sup>3</sup>	
	$\lambda_{\text{max}}$	fwhm	$\lambda_{\text{max}}$	fwhm	$\lambda_{\text{max}}$	fwhm
<b>Absorption</b>						
$a = 10, c = 10, 15, 30, 50^b$	643	65	648	74	650	76
$a = 10, 15, 30, c = 10$	643	65	648	74		
bulk	891	139	939	162	961	175
<b>Fluorescence</b>						
$a = 10, c = 10$	776	125	780	123	802	138
$a = 10, c = 15$	788	125	796	133	815	140
$a = 10, c = 30$	788	125	796	131	815	139
$a = 10, c = 50$	788	125	796	132		
$a = 15, c = 10$	783	123	807	136		
$a = 30, c = 10$	796	120	832	135		
bulk	1202	266	1278	285	1330	309

<sup>a</sup> The absorption spectra maxima and widths for the cavity systems are, within 1 nm, independent of cavity size. <sup>b</sup> Only for  $\rho = 1.4$  and 2.0 g/cm<sup>3</sup>.

30, and 50 Å are shown in Figure 6 for solution densities equal to (a) 1.4 and (b) 2.0 g/cm<sup>3</sup>; results are shown for  $a = 10$  Å and  $c = 10, 15,$  and 30 Å for (c)  $\rho = 2.2$  g/cm<sup>3</sup>. The peak absorption and fluorescence spectra wavelengths at the maximum and full widths at half-maximum are summarized in Table 3. The behavior of the absorption spectra are fairly independent of the size of the main semi-axis  $c$  for a fixed solution density. The positions of the maxima are shifted to longer wavelengths and the widths increase as the solution density increases. The fluorescence spectra have a different behavior: as the cavity geometry changes from spherical to ellipsoidal, the maximum intensity of the spectrum shifts to the red (longer wavelengths). However, for the prolate ellipsoidal cavities ( $a = 10$  Å,  $c = 15, 30, 50$  Å), the fluorescence spectrum changes little in position or width as the main semi-axis  $c$  increases for each of the solution densities.

In the present simulations, the fluorescence spectra for the prolate ellipsoidal cavities in Figure 6a shift to the red as the semi-axis  $c$  increases, but the effect quickly saturates. This is a different behavior than the one found for spherical cavities in ref 25, in which the fluorescence spectrum peak shifts consistently to the red as the cavity radius increases. The relative independence of the fluorescence spectra for the prolate ellipsoidal cavity with increasing size of the major semi-axis  $c$  implies a very similar environment of the solute in the excited state for all sizes of prolate ellipsoid cavities considered. The absorption and fluorescence spectra with higher density in Figures 6b and 6c follow a trend similar to that in Figure 6a with their maximum intensities shifted to the red due to the overall increase in the solvent polarity due to the higher density.

As in ref 25, the distribution of solute positions contributing to the absorption and fluorescence spectra are critical for interpreting the spectra. Thus, we postpone such an analysis of the spectra to section 4.3 where the solute probability densities are given.

**4.2.2. Oblate Ellipsoidal Cavities.** The absorption and fluorescence spectra for the solute molecule dissolved in CH<sub>3</sub>I confined in oblate ellipsoidal cavities with semi-axis  $c = 10$  Å and  $a = 10, 15,$  and 30 Å are shown in Figure 7 for solution densities equal to 1.4 and 2.0 g/cm<sup>3</sup>. The positions of the maxima and the widths of the absorption and fluorescence spectra for the oblate ellipsoidal cavities are summarized in Table 3. From Figure 7, it is clear that the behavior of the absorption spectra are fairly independent of the cavity size for

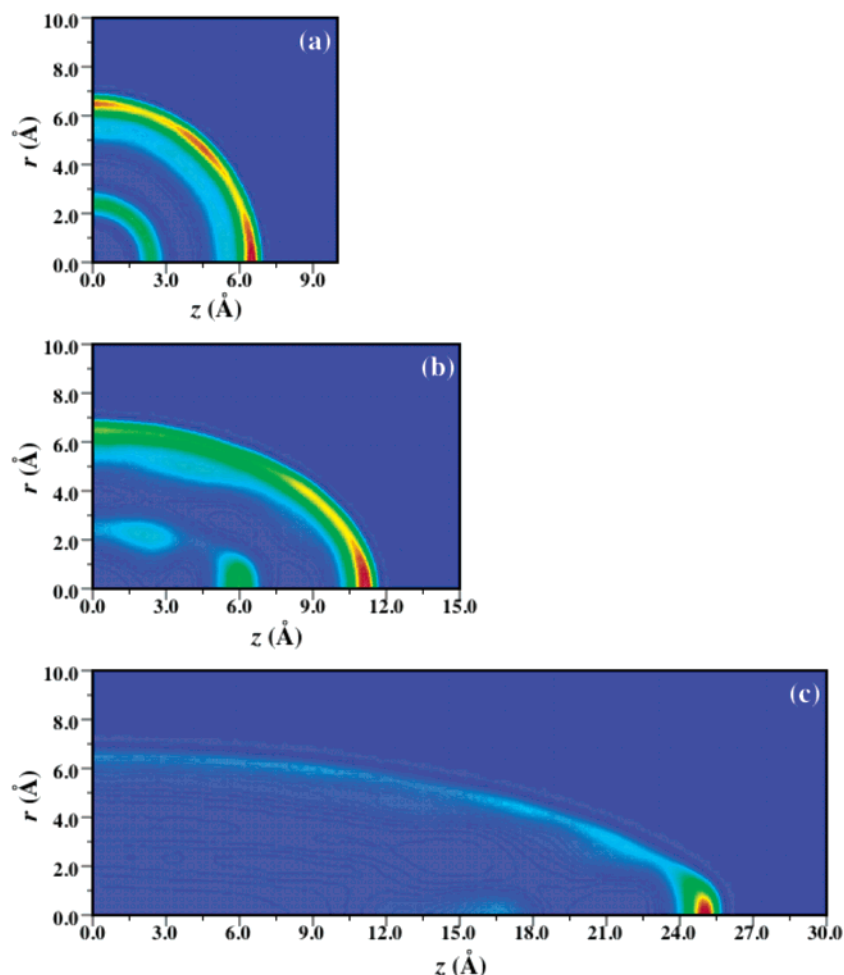


**Figure 9.** The probability density of the solute center-of-mass with the solute molecule in its ground state is shown for cavities with  $a = 10$  Å and  $c = 10, 15$ , and  $30$  Å (panels (a), (b), and (c), respectively) for a solution density of  $\rho = 2.0$  g/cm<sup>3</sup>. In each plot 100 contours are used between 0 (blue) and the maximum probability density (red) of (a)  $4.56 \times 10^{-3}$  Å<sup>-3</sup>, (b)  $3.57 \times 10^{-3}$  Å<sup>-3</sup>, and (c)  $6.54 \times 10^{-3}$  Å<sup>-3</sup>.

each solution density. From Table 3, we can see that for a fixed solution density the position of the maxima and the widths at the half-maximum of the absorption spectra for the oblate ellipsoidal cavities have approximately the same values as in spherical and prolate ellipsoidal cavities. The position of the maxima are shifted to longer wavelengths and the widths increase as the solution density increases. For the fluorescence spectra, different behavior is observed: as the semi-axis  $a$  increases, the position of the maximum intensity of the fluorescence spectrum shifts consistently to the red (longer wavelengths). The behavior of the fluorescence spectra is similar to that found for spherical cavities in ref 25. Thus, this behavior could be explained with the same arguments. Due to the large dipole of the solute in the excited state, it is mostly found in the interior of the cavity (see section 4.3) surrounded by a complete solvation shell, and as the cavity size increases the polarity in the environment of the solute increases. The fluorescence spectra for solution density of  $2.0$  g/cm<sup>3</sup> in Figure 7b follow the same trend but with their maximum intensities shifted to longer wavelengths.

**4.2.3. Bulk Solution.** The absorption and fluorescence spectra for the solute molecule in bulk CH<sub>3</sub>I solution (as approximated with periodic boundary conditions) are shown in Figure 8 for densities of  $1.4, 2.0$ , and  $2.2$  g/cm<sup>3</sup>. It is clear by comparison with Figures 6 and 7 that the cavities considered in this work are far from the bulk limit as evidenced by the considerable red shift of the spectra in the bulk relative to those in the cavities. This result is not surprising given the dimensions of the cavity

and the absence of long-range electrostatic interactions. Note that both the absorption and fluorescence spectra shift to longer wavelengths as the density increases as was also observed in the cavity systems.

**4.3 Solute Probability Density.** **4.3.1. Prolate Ellipsoidal Cavities.** The probability densities of the solute center-of-mass for the solution density of  $2.0$  g/cm<sup>3</sup> as a function of the cylindrical coordinates  $z$  and  $r$  (see section 3.2) in prolate ellipsoidal cavities with semi-axis  $a$  fixed to  $10$  Å and semi-axis  $c$  equal to  $10, 15$ , and  $30$  Å are shown in Figures 9 and 10 for the solute in the ground and excited states, respectively. These probability densities are normalized to unity so that the integral of the probability density over all the elemental volumes  $2\pi r dz dr$  is equal to one.

For the spherical cavity ( $a = 10$  Å,  $c = 10$  Å), the probability density of the solute center-of-mass has spherical symmetry (within statistical error) around the center of the cavity for the solute in the ground (Figure 9a) and excited (Figure 10a) states. In the ground state we can see that the solute is most likely to be found near the cavity wall and, with a much lower probability, nearer the center of the spherical cavity (Figure 9a). For the prolate ellipsoidal cavities (Figures 9b and 9c), the most probable region is also near the cavity wall, but in these cases there appear peaks of maximum probability at the “end” of the ellipsoid along semi-axis  $c$  (here maximum  $z$ ). Smaller peaks in the probabilities are also found in the interior of the cavity along the main semi-axis around  $z = 6$  and  $16.5$  Å for cavities with  $c = 15$  and  $30$  Å, respectively.



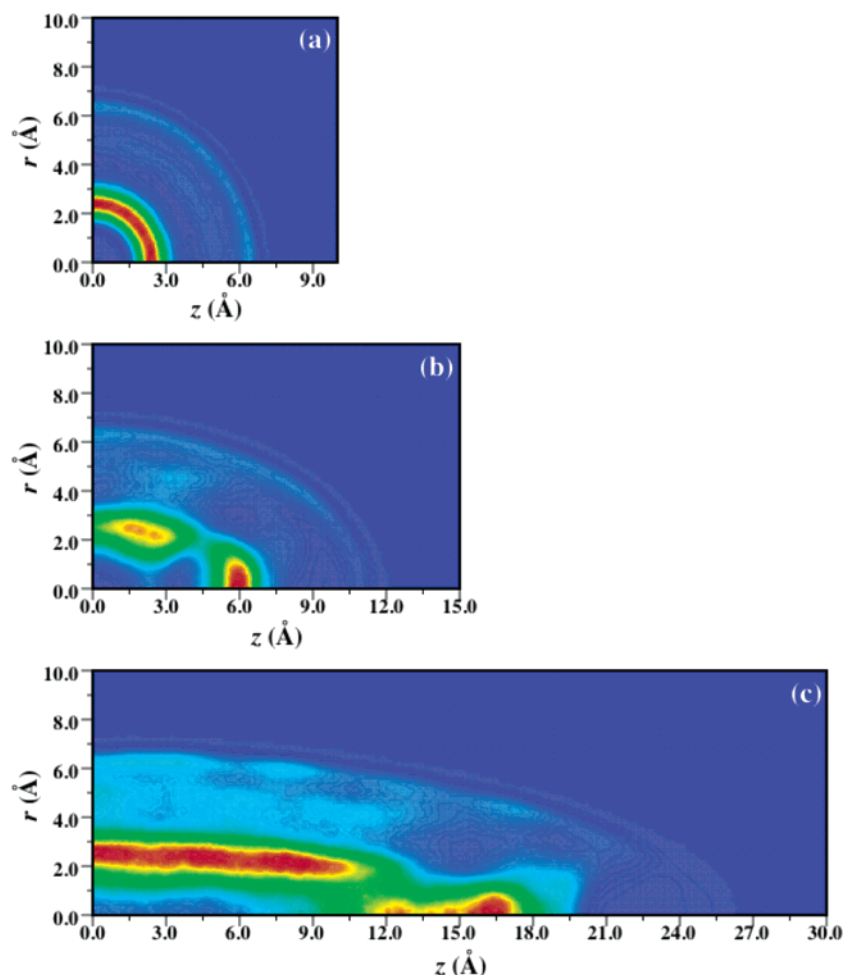


**Figure 10.** The probability density of the solute center-of-mass with the solute molecule in its excited state is shown for cavities with  $a = 10$  Å and  $c = 10, 15$ , and  $30$  Å (panels (a), (b), and (c), respectively) for a solution density of  $\rho = 2.0$  g/cm<sup>3</sup>. In each plot 100 contours are used between 0 (blue) and the maximum probability density (red) of (a)  $12.59 \times 10^{-3}$  Å<sup>-3</sup>, (b)  $5.99 \times 10^{-3}$  Å<sup>-3</sup>, and (c)  $1.82 \times 10^{-3}$  Å<sup>-3</sup>.

From the probability density of the solute in the excited state in Figure 10, it is observed that for the spherical cavity (Figure 10a), the position of the solute molecule is most probably in the cavity interior; there is a significantly smaller probability for the molecule to be found near the cavity wall (see ref 25). For the prolate ellipsoidal cavities (Figures 10b and 10c), the probability density of the solute is also high in the interior of the cavity. Note that the layered structure in the solute probability densities is correlated with the solvent structure shown in Figure 3. In the ground state the solute is found primarily in the solvent layer nearest the cavity wall, while in the excited state it is mostly present in the inner layer of solvent molecules.

The different behavior of the solute molecule in its ground and excited states can only be due to the electrostatic interactions with the solvent. Since the solute in the ground state is mostly near the cavity wall, it is only partially surrounded by solvent molecules. This is reflected in the absorption spectra (Figure 6b), in which the most contributions come from the environment of the solute molecule with a partial solvation shell and does not change much with cavity size. In contrast, the solute molecule in the excited state is most likely to be in the interior of the cavity, the larger solute dipole moment is better solvated in the interior of the cavity surrounded by a complete shell of solvent molecules.<sup>25</sup> This is reflected in Figure 6b, which shows the fluorescence spectra for the prolate ellipsoidal cavities shifted to longer wavelengths relative to that in the spherical cavity. However, the spectra for all the ellipsoidal cavities is essentially

the same, indicating little change in the solute environment with the increasing of the semi-axis  $c$ .

In previous work on the same system confined in spherical cavities of radii 10, 12, 15, and 20 Å for a solution density of 1.4 g/cm<sup>3</sup>, we found that the absorption spectra change little with increasing cavity radius;<sup>25</sup> the maximum intensities and widths were fairly independent of the cavity size with approximate values of 643 and 65 nm, respectively. The present simulations give the same results for the absorption spectra in spherical and prolate ellipsoidal cavities for a solution density of 1.4 g/cm<sup>3</sup>. Thus, it is clear that the absorption spectrum is not sensitive to the geometry and size of the cavity for a fixed density. The behavior of the absorption spectra can be explained with the same arguments as in ref 25: the solute molecules contributing to the absorption spectra are primarily found next to the cavity wall due to the low dipole moment of the ground state and the polarity of the solvent. Thus, the solute environment consists only of a partial solvation shell and does not change greatly with cavity size.

Also in ref 25, the fluorescence spectra for the same system as in the present work confined in spherical cavities with density 1.4 g/cm<sup>3</sup> were simulated. It was found that the fluorescence spectra shift steadily to the red with increasing cavity radius. This is consistent with the idea that the confined solvent polarity increases with the cavity size.<sup>23</sup> In contrast to the absorption spectrum which probes ground state solute molecules, the fluorescence spectrum provides information about the excited state solute which, due to the large solute dipole moment, is

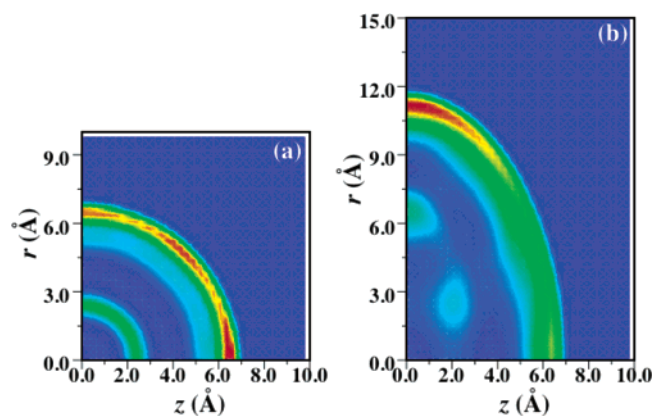


**Figure 11.** The probability density of the solute center-of-mass with the solute molecule in its ground state is shown for cavities with  $c = 10$  Å and (a)  $a = 10$  Å and (b)  $a = 15$  Å for a solution density of  $\rho = 2.0$  g/cm<sup>3</sup>. In each plot 100 contours are used between 0 (blue) and the maximum probability density (red) of (a)  $4.56 \times 10^{-3}$  Å<sup>-3</sup> and (b)  $1.59 \times 10^{-3}$  Å<sup>-3</sup>.

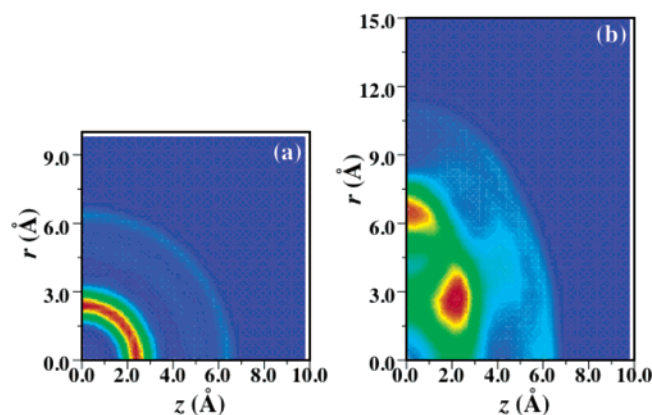


**Figure 12.** The probability density of the solute center-of-mass with the solute molecule in its excited state is shown for cavities with  $c = 10$  Å and (a)  $a = 10$  Å and (b)  $a = 15$  Å for a solution density of  $\rho = 2.0$  g/cm<sup>3</sup>. In each plot 100 contours are used between 0 (blue) and the maximum probability density (red) of (a)  $12.59 \times 10^{-3}$  Å<sup>-3</sup> and (b)  $2.28 \times 10^{-3}$  Å<sup>-3</sup>.

found primarily in the cavity interior surrounded by a complete solvation shell. Thus, the absorption and fluorescence spectra illustrate the importance and variability of the solute position. In this model system, because of the difference in ground and excited-state solute position distributions, the fluorescence spectrum is more sensitive to any change in solvent polarity, e.g., through increasing the cavity size, while the absorption spectrum is essentially unchanged. However, for the prolate ellipsoidal cavities considered, the environment of the excited state solute, which lies primarily in the cavity interior, is relatively insensitive to the semi-axis  $c$ . Instead, in this location the solute fluorescence spectrum is controlled by the  $a$  semi-axis; crudely, these simulations indicate a rapid onset of the cylindrical limit.

**4.3.2. Oblate Ellipsoidal Cavities.** The probability densities of the solute center-of-mass for a solution density of  $2.0$  g/cm<sup>3</sup> in oblate ellipsoidal cavities with semi-axis  $a$  equal to 10 and 15 Å and semi-axis  $c$  fixed to 10 Å are shown in Figures 11 and 12 for the solute in the ground and excited states, respectively. For the ground-state solute in the oblate ellipsoidal cavity (Figure 11b), the most probable position is also near the cavity wall with the highest peak around the coordinates  $z = 0$  and  $r = 11.5$  Å for the  $a = 15$  Å cavity (again at the “ends” of the ellipsoid). In contrast, the excited-state solute (Figure 12b)

is most likely found in the cavity interior where the larger charges are better solvated.

We can see that the position distributions of the solute center-of-mass in oblate ellipsoidal cavities are similar to those in prolate ellipsoidal cavities. Namely, the solute molecule in the ground state is most likely to be near the cavity wall partially surrounded by the solvent. The excited state solute is better solvated in the interior of the cavity surrounded by a complete shell of solvent. The primary difference is that in the oblate ellipsoidal cavities one increases the size in the direction of two semi-axes instead of only one as in the prolate case. Thus, the environment experienced by the excited solute molecule near the cavity center *does* change significantly as the cavity dimensions are increased. This is reflected in Figure 7, which shows the fluorescence spectrum shifting consistently to the red as the cavity size (i.e., semi-axis  $a$ ) increases.

## 5. Conclusions

Monte Carlo simulations have been used to calculate the absorption and fluorescence spectra of a model diatomic solute (with a charge-transfer transition) in a methyl iodide solvent confined in nanoscale ellipsoidal cavities. In addition, the solute and solvent (center-of-mass) probability distributions have been calculated and used to interpret the spectra. The solute distributions have been obtained with the weighted histogram analysis method of Kumar et al.<sup>33</sup> based on umbrella sampling. The effect of breaking the spherical symmetry of the confining cavity has been probed by considering both prolate and oblate ellipsoidal cavities of varying size. The role of solvent density has also been examined.

As was found previously in spherical cavities,<sup>25</sup> the absorption spectrum for the model solute is insensitive to the cavity dimensions. The absorption spectra shown in Figures 6 and 7 are essentially the same for all the spherical, prolate, and oblate cavities (see also Table 3). In contrast, in the fluorescence spectra (Figure 6) for the prolate ellipsoidal cavities considered in this work ( $a = 10$  Å,  $c = 15, 30, 50$  Å), the maximum peak shifts to the red with the increasing of the semi-axis  $c$ , but it quickly becomes independent of the main semi-axis size. For the oblate ellipsoidal cavities ( $a = 10, 15, 30$  Å,  $c = 10$  Å), the fluorescence spectra (Figure 7) shift to the red steadily as the semi-axis  $a$  increases, as was found for spherical cavities.<sup>25</sup>

The unusual spectral shifts with cavity size in the spherical cavity case were attributed to differences between the solute position distributions in the ground and excited states that are probed by the absorption and fluorescence, respectively.<sup>25</sup> Namely, the low dipole moment in the ground state leads to a position distribution peaked near the hydrophobic cavity wall while the more polar excited state is found predominantly in the cavity interior fully surrounded by solvent molecules. The fluorescence spectrum is therefore more sensitive to changes in the solvent polarity than is the absorption spectrum. The present results indicate that the same analysis can be used to explain the spectra in ellipsoidal cavities. A new feature, however, is that the effective solvent polarity in the cavity interior is limited by the minor semi-axes  $a$  for prolate cavities leading to a rapid saturation in the fluorescence red shift with increasing major semi-axis  $c$ . In the oblate ellipsoid case, as the semi-axes  $a$  are increased, the semi-axis  $c$  does not limit the effective solvent polarity and a consistent fluorescence red shift is observed.

It is important to note that the solute positions are also affected by the solvent structure in the cavities. Specifically, the solvent

packs in “layers” separated roughly by the van der Waal diameter of the solvent molecule (here  $\sim 4$  Å). The layering of a liquid at the interface with a solid surface is a well-known phenomenon that was observed previously in spherical cavities.<sup>25,26</sup> The local solvent density in these layers increases as the total solution density in the cavity increases (see Figure 4). In addition, as the major semi-axis  $c$  is increased in the prolate ellipsoidal cavities, the solvent density approaches cylindrical symmetry near the cavity interior (small  $z$ ). The solvent density naturally affects the solute position distributions leading to layered structures and a significant density in the solute ground state to be found near the ellipsoid “ends” where the solvent density is smaller.

**Acknowledgment.** This work was supported by the Chemical Sciences, Geosciences and Biosciences Division, Office of Basic Energy Sciences, Office of Science, U.S. Department of Energy.

## References and Notes

- (1) Brinker, C. J.; Scherer, G. W. *Sol–Gel Science: The Physics and Chemistry of Sol–Gel Processing*; Academic Press: New York, 1990.
- (2) See, e.g., Fendler, J. H. *J. Phys. Chem.* **1980**, *84*, 1485–1491. Pileni, M. P., Ed.; *Structure and Reactivity in Reverse Micelles*; Elsevier: New York, 1989.
- (3) See, e.g., Rebek, J., Jr. *Acc. Chem. Res.* **1999**, *32*, 278–286. MacGillivray, L. R.; Atwood, J. L. *Adv. Supramolec. Chem.* **2000**, *6*, 157–183. Steed, J. W.; Atwood, J. L. *Supramolecular Chemistry*; Wiley: New York, 2000.
- (4) A recent example is Gu, L.-Q.; Cheley, S.; Bayley, H. *Science* **2001**, *291*, 636–640.
- (5) See, e.g., De Vos, D. E.; Dams, M.; Sels, B. F.; Jacobs, P. A. *Chem. Rev.* **2002**, *102*, 3615–3640.
- (6) Bhattacharyya, K.; Bagchi, B. *J. Phys. Chem. A* **2000**, *104*, 10603–10613.
- (7) Zhang, J.; Jonas, J. *J. Phys. Chem.* **1993**, *97*, 8812–8815. Korb, J.-P.; Xu, S.; Jonas, J. *J. Chem. Phys.* **1993**, *98*, 2411–2422. Korb, J.-P.; Malier, L.; Cros, F.; Xu, S.; Jonas, J. *Phys. Rev. Lett.* **1996**, *77*, 2312–2315. Korb, J.-P.; Xu, S.; Cros, F.; Malier, L.; Jonas, J. *J. Chem. Phys.* **1997**, *107*, 4044–4050.
- (8) Loughnane, B. J.; Fourkas, J. T. *J. Phys. Chem. B* **1998**, *102*, 10288–10294. Loughnane, B. J.; Scodinu, A.; Fourkas, J. T. *J. Phys. Chem. B* **1999**, *103*, 6061–6068. Loughnane, B. J.; Farrer, R. A.; Scodinu, A.; Reilly, T.; Fourkas, J. T. *J. Phys. Chem. B* **2000**, *104*, 5421–5429. Farrer, R. A.; Fourkas, J. T. *Acc. Chem. Res.* **2003**, *36*, 605–612.
- (9) Streck, C.; Mel’nichenko, Y. B.; Richert, R. *Phys. Rev. B* **1996**, *53*, 5341–5347. Richert, R. *Phys. Rev. B* **1996**, *54*, 15762–15766.
- (10) Pal, S. K.; Sukul, D.; Mandal, D.; Sen, S.; Bhattacharyya, K. *J. Phys. Chem. B* **2000**, *104*, 2613–2616.
- (11) Wang, H.; Bardo, A. M.; Collinson, M. M.; Higgins, D. A. *J. Phys. Chem. B* **1998**, *102*, 7231–7237. Mei, E.; Bardo, A. M.; Collinson, M. M.; Higgins, D. A. *J. Phys. Chem. B* **2000**, *104*, 9973–9980.
- (12) Baumann, R.; Ferrante, C.; Deeg, F. W.; Bräuchle, C. *J. Chem. Phys.* **2001**, *114*, 5781–5791. Baumann, R.; Ferrante, C.; Kneuper, E.; Deeg, F. W.; Bräuchle, C. *J. Phys. Chem. A* **2003**, *107*, 2422–2430.
- (13) Sarkar, N.; Das, K.; Datta, A.; Das, S.; Bhattacharyya, K. *J. Phys. Chem.* **1996**, *100*, 10523–10527.
- (14) Riter, R. E.; Willard, D. M.; Levinger, N. E. *J. Phys. Chem. B* **1998**, *102*, 2705–2714. Pant, D.; Riter, R. E.; Levinger, N. E. *J. Chem. Phys.* **1998**, *109*, 9995–10003. Riter, R. E.; Undiks, E. P.; Kimmel, J. R.; Levinger, N. E. *J. Phys. Chem. B* **1998**, *102*, 7931–7938. Willard, D. M.; Ritter, R. E.; Levinger, N. E. *J. Am. Chem. Soc.* **1998**, *120*, 4151–4160. Willard, D. M.; Levinger, N. E. *J. Phys. Chem. B* **2000**, *104*, 11075–11080. Pant, D.; Levinger, N. E. *Langmuir* **2000**, *16*, 10123–10130. Riter, R. E.; Undiks, E. P.; Levinger, N. E. *J. Am. Chem. Soc.* **1998**, *120*, 6062–6067. Riter, R. E.; Kimmel, J. R.; Undiks, E. P.; Levinger, N. E. *J. Phys. Chem. B* **1997**, *101*, 8292–8297.
- (15) Brown, D.; Clarke, J. H. R. *J. Phys. Chem.* **1988**, *92*, 2881–2888.
- (16) Linse, P. *J. Chem. Phys.* **1989**, *90*, 4992–5004. Linse, P.; Halle, B. *Mol. Phys.* **1989**, *67*, 537–573.
- (17) Faeder, J.; Ladanyi, B. M. *J. Phys. Chem. B* **2000**, *104*, 1033–1046.
- (18) Faeder, J.; Ladanyi, B. M. *J. Phys. Chem. B* **2001**, *105*, 11148–11158.
- (19) Das, K.; Sarkar, N.; Das, S.; Datta, A.; Bhattacharyya, K. *Chem. Phys. Lett.* **1996**, *249*, 323–328.
- (20) Nandi, N.; Bagchi, B. *J. Phys. Chem.* **1996**, *100*, 13914–13919.
- (21) See, e.g., Ping, G.; Yuan, J. M.; Vallieres, M.; Dong, H.; Sun, Z.; Wei, Y.; Li, F. Y.; Lin, S. H. *J. Chem. Phys.* **2003**, *118*, 8042–8048. Friedel, M.; Sheeler, D. J.; Shea, J.-E. *J. Chem. Phys.* **2003**, *118*, 8106–8113.
- (22) Senapati, S.; Chandra, A. *J. Chem. Phys.* **1999**, *111*, 1223–1230.
- (23) Senapati, S.; Chandra, A. *J. Chem. Phys. B* **2001**, *105*, 5106–5109.
- (24) Turner, C. H.; Brennan, J. K.; Johnson, J. K.; Gubbins, K. E. *J. Chem. Phys.* **2002**, *116*, 2138–2148.
- (25) Thompson, W. H. *J. Chem. Phys.* **2002**, *117*, 6618–6628.
- (26) Thompson, W. H. *J. Chem. Phys.* **2004**, *120*, 8125–8133.
- (27) Freitas, F. F. M.; Fernandes, F. M. S. S.; Cabral, B. J. C. *J. Phys. Chem.* **1995**, *99*, 5180–5186.
- (28) See, e.g., McQuarrie, D. A. *Statistical Mechanics*; HarperCollins: New York, 1976.
- (29) Press, W. H.; Flannery, B. P.; Teukolsky, S. A.; Vetterling, W. T. *Numerical Recipes*; Cambridge University Press: New York, 1986.
- (30) Haselgrove, C. B. *Math. Comput.* **1961**, *15*, 323–337.
- (31) Allen, M. P.; Tildesley, D. J. *Computer Simulation of Liquids*; Oxford University Press: New York, 1987.
- (32) Frenkel, D.; Smit, B. *Understanding Molecular Simulation, from Algorithms to Applications*; Academic Press: New York, 1996.
- (33) Kumar, S.; Bouzida, D.; Swendsen, R. H.; Kollman, P. A.; Rosenberg, J. M. *J. Comput. Chem.* **1992**, *13*, 1011–1021. Kumar, S.; Bouzida, D.; Swendsen, R. H.; Kollman, P. A.; Rosenberg, J. M. *J. Comput. Chem.* **1995**, *16*, 1339–1350.
- (34) Torrie, G. M.; Valleau, J. P. *J. Comput. Phys.* **1977**, *23*, 187–199.